# γ-Ray-Assisted Synthesis of a Pt−Sn *Bimetallic* Composite Loaded on Graphene−Graphitic Carbon Nitride Hybrid: A Cocktail Electrocatalyst for the Methanol Oxidation Reaction

Durgasha C. Poudyal, Rajshree Dugani, Banendu Sunder Dash, Manjiri Dhavale, Ashis Kumar Satpati, and Santosh K. Haram*

Read Online

ACCESS | Metrics & More | Article Recommendations | SI Supporting Information

**ABSTRACT:** The composite of Pt with transition metals is viewed as the most promising anode material for direct methanol fuel cell (DMFC) applications. Besides the decrease in the Pt loading, these multimetallic structures help in circumventing CO poisoning issues associated with a Pt catalyst. Herein, we prepared and loaded Pt−Sn bimetallic nanoparticles on an electron-rich and stable substrate consisting of graphitic nitride (GCN) and graphene oxide (GO)/reduced graphene oxide (r-GO) hybrid composites. The γ-radiolysis method was employed for coreduction of metal salts to deposit the binary composite of metal nanoparticles over the substrates. These structures were tested as the anode material for the methanol oxidation reaction (MOR). Among various possible combinations, Pt−Sn-loaded rGO-GCN (Pt−Sn/rGO-GCN) demonstrated the current density of ca. 2.4 A/mg$_{Pt}$. To the best of our knowledge, this value is among the highest ones, reported for similar systems in the acidic pH. Furthermore, these composites demonstrated excellent stability in the repeated cycle test. The improved performance is associated to the plenty of −OH groups provided by the Sn counterpart and a large number of adsorption sites from the electron-reached GCN counterpart.
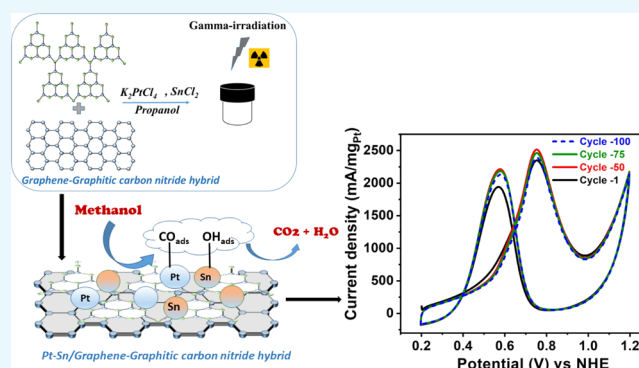
## 1. INTRODUCTION

Polymer electrolyte membrane fuel cells (PEMFCs) have been emerged as a promising low-temperature system (<150 °C) to convert fuel directly into electricity. Although this technology has been reached to a commercial production level, the difficulty in onboard handling and storage of inflammable H$_2$ gas has still remained as a challenge for its mobile applications.[1−3] Reforming liquid fuel into H$_2$ and using it immediately in PEMFCs have been tested previously.[4] However, its economical viability is in question due to high operation temperature, high pay load, and challenges with effective separation of H$_2$ gas from CO/CO$_2$. However, another proposition is to use liquid fuel "directly" into PEMFCs, without much alteration in the basic architecture of the cell. In this context, a direct methanol fuel cell (DMFC) has emerged as a novel possibility.[2,5] In recent years, DMFCs have been tried and tested as an alternative to diesel generators and battery backups employed in off-grid applications such as telecommunications and portable applications.[6]

Methanol as a fuel has many advantages over gaseous hydrogen, viz., safe to handle, high hydrogen content, and readily available from many naturally derivable sources, viz., coal, biowaste, and bagasse. However, the poisoning of Pt by oxidative intermediates such as CO, formed during MOR,[7,8] is

among major challenges which are mitigated using Ru[9] as a cocatalyst—albeit with much added cost. The Ru counterpart provides abundant surface hydroxyl groups in acidic pH which helps in oxidizing the adsorbed CO and other intermediates, thereby relieving Pt active sites available for the next oxidation cycles.[10] Recently, several other strategies have been followed to decrease the cost by substituting Ru with less-expensive transition-metal combinations, viz., Pt−Sn,[11] Pt−Cu,[12] Pt−Ru−Mo,[13] and Pt−Co.[14] Among them, Pt−Sn displayed better performance due to its formation of stable multioxidation states and can provide abundant hydroxyl groups even in acidic pH like Ru.

Besides the active metal parts, the efficiency of MOR and stability of catalysts are equally influenced by the type of the substrates.[3] Carbon-based materials are preferred substrates due to their high specific surface area and superior thermal

conductivity, without compromising electron mobility.[15] Vulcan carbon (XC-72), graphene, and carbon nanotubes have been tested thoroughly as substrates for MOR electrocatalysts;[3] however, the carbon supports suffer from oxidative corrosion in the acidic pH, which lead to the agglomeration and leaching of active metal parts. The leaching effect is also attributed to the poor interaction of the metal counterpart with carbon due to insufficient unsaturation on the graphitic surface.

Recent studies suggest that the incorporation of the heteroatoms such as N in the graphitic structure, viz., graphitic carbon nitride (GCN), N-doped graphene not only helps in adhering metal nanoparticles but also enhances the performance by providing specific adsorption centers.[16] Hence, GCN and N-doped graphene have been widely studied for various electrocatalytic and photocatalytic applications.[17] Thus, to improve the electric properties, GCN is often used in combination with r-GO.[18] With these notions, Pt-loaded 3D graphene/graphitic carbon nitride architectures have been tested and these combinations demonstrated high electrocatalytic activity, CO tolerance, and stability, superior to those of commercial Pt-Vulcan XC-72 (Pt/C) and Pt-graphene (Pt/G) hybrids.[19] Similarly, 3D hierarchically porous carbon nanostructure supports are proved to be the excellent support material and Pt-g-$C_3N_4$-rGO has exhibited a good performance for MOR.[18] Although substantial work has been carried out on Pt metal particles loaded on GCN/GO combinations, to our knowledge, there is seldom any report on the bimetallic catalysts loaded on the GCN/GO and tested for MOR. Such a combination is expected to perform better than Pt/GCN/GO alone.

Herein, we report a unique synthetic approach for the preparation of Pt–Sn metal catalysts, loaded on the rGO-GCN hybrid support. Here, Sn was chosen as a cocatalyst over Ru because of its earth abundance and having multiple stable oxidation states which are known to provide a large number of −OH groups even in the acidic pH. The novelty of the present work is the application of the γ-radiolysis method for the coreduction of Pt and Sn salts on the substrate. The γ-radiolysis method is known for a cleaner reduction of metal salts, without leaving any residue of byproducts on the catalyst surface. The highlight of the work is superior performance displayed by Pt–Sn-loaded rGO-GCN for MOR in terms of current, potential, and stability as compared to the Pt alone loaded on rGO-GCN, GO/GCN, and commercial Pt 20%/C catalysts.

## 2. RESULTS AND DISCUSSION

### 2.1. Preparation of the Composites.
Pt and Sn nanoparticles and their bimetallic composite were deposited on the hybrid support by reducing their respective salts by γ-radiolysis. The plausible mechanism involves the formation of the hydroxyl and hydrogen radicals as radiolysis products. Hydroxyl radicals get scavenged by propanol which leaves steady concentration of hydrated electrons in the solution.[7,20] These electrons are known to be responsible for the reduction. The heterogeneities on the supports (GO/GCN) provide the nucleation sites for the metal clusters which further facilitate nanoparticle formation. The hydrated electrons may also reduce part of the GO.

The products were characterized using various techniques described below.

### 2.2. Characterization of Composites.
FTIR spectral analysis was used as a tool to investigate functional groups

associated with the hybrid supports (GO, rGO, and GO-GCN). The results are shown in Figure 1.
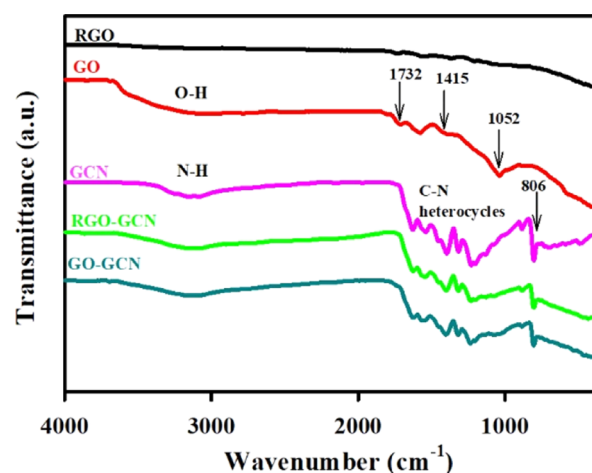


**Figure 1.** FTIR spectra recorded for the individual RGO, GO, and GCN samples and their hybrids, viz., rRGO-GCN and GO-GCN. The relevant bands are marked for more clarity.

The spectra for GO prominently show the bands due to oxygenated functionalities, viz., C=O (at 1732 cm$^{-1}$), C−OH (1418 cm$^{-1}$), C−O (1051 cm$^{-1}$), and OH (broad peak 3000−3500 cm$^{-1}$). In the case of rGO, the band due to O−H stretching (∼3400 cm$^{-1}$) was decreased compared to the precursor (GO) due to its deoxygenation during the reduction reaction. Nevertheless, the C−O stretching remains unaffected during the reduction.[21]

In the case of GCN, the narrow band at 806 cm$^{-1}$ is attributed to the breathing mode of the triazine ring. The bands at 1200−1700 cm$^{-1}$ are attributed to the characteristic stretching modes of CN heterocycles. The band in the range 3000−3600 cm$^{-1}$ is assigned to the N−H stretching.[17] The spectra of hybrid samples, viz., GO-GCN and rGO-GCN, show neither shift in the original band positions nor appearance of additional bands.

Figure 2A−D shows the field emission scanning electron microscopy (FESEM) images of Pt/GO-GCN, Pt−Sn/GO-GCN, Pt/rGO-GCN, and Pt−Sn/rGO-GCN, respectively. The corresponding images for the controlled samples (substrates, before loading metal parts) are presented in Supporting Information Figure S1A,B. Typical layered morphology associated to the graphitic backbone is seen as a common feature in all the micrographs. The nanoparticles deposited on the graphitic structure are legible as bright spots in Figure 2A−D. In the case of Pt loaded on GO-GCN (Figure 2A), a large number of particles are noted to be agglomerated, while in the case of Pt−Sn/rGO-GCN (Figure 2D), the nanoparticles are dispersed more or less uniformly on the surface and at the edges. Overall, the Pt−Sn nanoparticles on rGO-GCN (Figure 2D) show more uniform dispersion and better loading on the hybrid support as compared to Pt−Sn on GO-GCN (Figure 2B). This observation is attributed to the excess electron density associated with r-GO which plausibly induces uniform nucleation and growth of nanoparticles. From the EDAX (refer Figure S2 Supporting Information) and ICP-OES analysis (refer Table S1, Supporting Information), the ratio of Pt−Sn for rGO-GCN and GO-GCN was found to be 2:1 and 1:4, respectively.
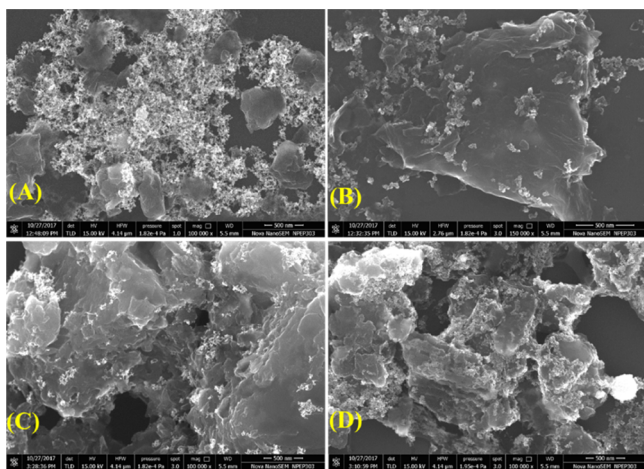
**Figure 2.** FESEM of (A) Pt/GO-GCN, (B) Pt−Sn/GO-GCN, (C) Pt/rGO-GCN, and (D) Pt−Sn/rGO-GCN. In the micrographs (A−C), the agglomeration of metal nanoparticles on edge sites is noted. (D) Uniform distribution of Pt−Sn NPs.

To gain further insights into the morphology and to estimate an average particle size, transmission electron microscopy (TEM) investigations were performed on the samples. Figure 3A,B shows typical micrographs recorded on Pt−Sn/rGO-
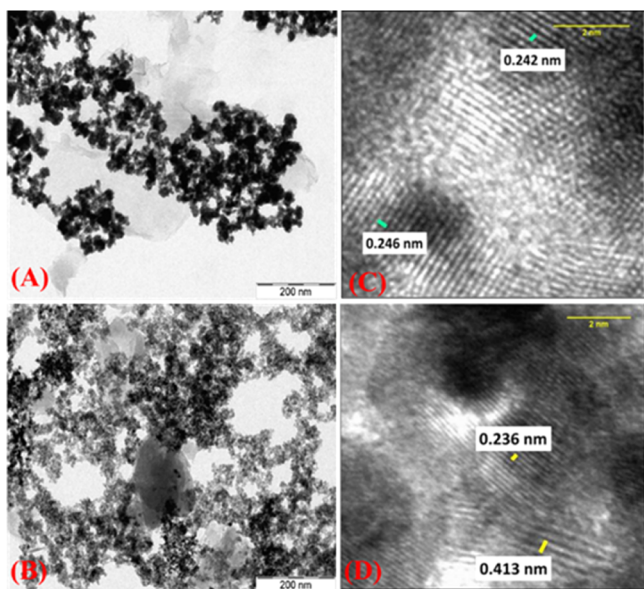


**Figure 3.** TEM images for (A) Pt/GO-GCN and (B) Pt−Sn/rGO-GCN. (C,D) Respective lattice fringes.

GCN and Pt/GO-GCN samples, respectively. Dark-contrasted dots observed in the micrographs are indicative of metal NP parts, while the graphene is seen as a light-gray semitransparent layered structure in the background. From the micrographs, the average size of the nanoparticles is estimated to be 5−10 nm. Upon careful observation, two distinct contrast values were noted within the nanoparticle portion; the one with darker contrast is attributed to the relatively high atomic number element, that is, Pt, while the less dark one is attributed to Sn. Figure 3C,D represents lattice fringes recorded on the selected area of the samples. A predominant interplanar spacing of 0.246 nm is attributed to the Pt(111) indices, while 0.413 nm corresponds to Sn (100) indices.

In order to gain information on the surface composition and the oxidation state of the elements, X-ray photoelectron spectroscopy (XPS) analysis was performed. The presence of Pt, Sn, C, and N is noted in the survey scan, as shown in Figures 4A and S3A,B (Supporting Information). The high-
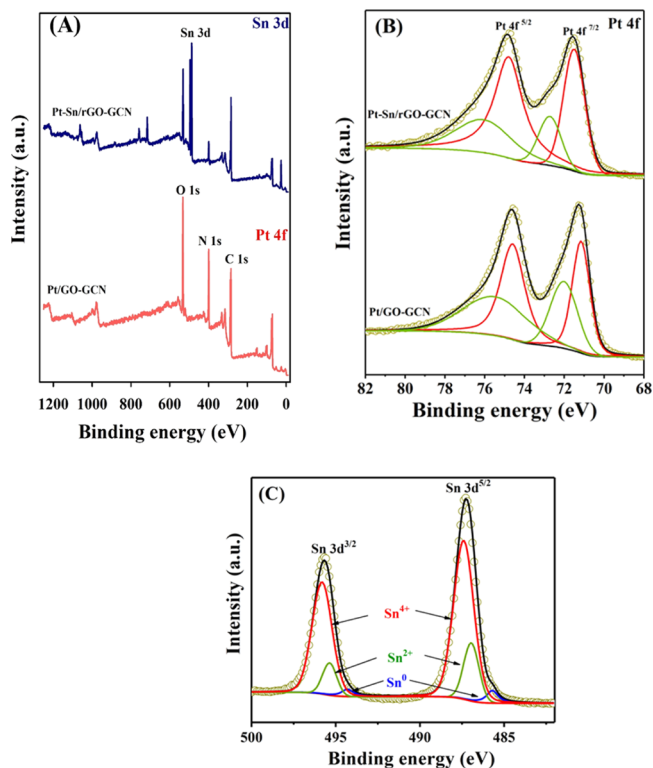


**Figure 4.** XPS recorded on the Pt−Sn/rGO-GCN composite. (A) Survey scan and (B) Pt 4f region of Pt/GO-GCN and Pt−Sn/rGO-GCN, respectively. (C) Sn 3d region. The circles are experimental data and black lines are fitting from deconvolution analysis (red, green, and blue lines).

resolution Pt 4f region (Figure 4B) shows splitting due to the spin−orbital coupling. These peaks were deconvoluted and assigned to $Pt^0$ having binding energy 71.3 and 74.7 eV and $Pt^{2+}$ having binding energy 72.2 and 76.2 eV. Deconvolution analysis in the $3d_{5/2}$ and $3d_{3/2}$ of the Sn region is shown in Figure 4C. It suggests a best fit of the data into three peaks, corresponding to $Sn^0$, $Sn^{2+}$, and $Sn^{4+}$ oxidation states. The stronger peaks at 487.4 eV ($3d_{5/2}$) and 495.8 eV ($3d_{3/2}$) are attributed to the $Sn^{4+}$ oxidation. The next intense peaks at 486.9 and 495.3 eV ($3d_{5/2}$ and $3d_{3/2}$) are attributed to the $Sn^{2+}$ oxidation state. The remaining weak peaks at 485.7 and 494.2 eV are matched very well with the $Sn^0$ oxidation state. All the binding energy values are in good agreement with the literature reports.[23,24] These data suggest that in the Pt−Sn nano-composite prepared by the γ-radiolysis, Sn is present predominately in the $Sn^{4+}$ oxidation state.

Similarly, deconvolution of the C 1s part is fitted into components having binding energy values 84.6 eV (sp2 C−C), 284.2 eV (C=C), 286.1 eV (C−OH), 286.98 eV (C−N), and 288.3 eV (C=O). The high-resolution N 1s spectrum is fitted into several peaks corresponding to C−N=C (399.2 eV), N−(C)3 (400.6 eV), and C−N (404.9 eV), and a hump at around 397.9 eV indicated a strong interaction between graphene and graphitic carbon nitride (Figure S3 Supporting Information).[17]
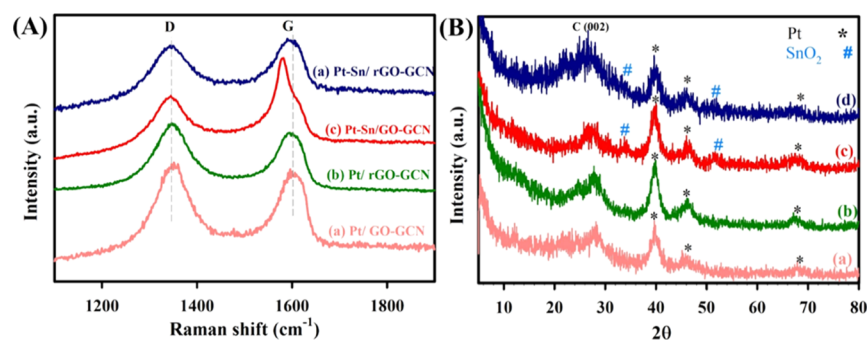
**Figure 5.** (A) Raman spectra and (B) powder XRD recorded for (a) Pt/GO-GCN, (b) Pt/rGO-GCN, (c) P−Sn/GO-GCN, and (d) Pt−Sn/rGO-GCN hybrids.

Figure 5A shows Raman spectra recorded for Pt/GO-GCN, Pt−Sn/GO-GCN, Pt/rGO-GCN, and Pt−Sn/rGO-GCN hybrids. The corresponding spectra for GO-GCN, Sn/GO-GCN, rGO-GCN, and Sn/rGO-GCN are shown in the Supporting Information (Figure S4). From those spectra, the hybrid GO-GCN shows the D and G bands at 1345 and 1595 cm$^{-1}$, respectively. After the reduction (rGO-GCN hybrid), the position of the D band remained unchanged, while the G band is downshifted to 1585 cm$^{-1}$. This change in the G band position is attributed to the re-establishment of the conjugated graphene network (sp$^2$ carbon), due to reductive removal of oxygen functionalities. The increase in the $I_D/I_G$ ratio from 0.74 (GO-GCN) to 1.01 (rGO-GCN) is attributed to the formation of more defect sites upon removal of oxygen.[25] Further increase in the $I_D/I_G$ ratio is observed for metal-loaded samples, that is, for Sn/GO-GCN (0.92), Pt/GO-GCN (1.03), and Pt−Sn/GO-GCN (0.88) than GO-GCN (0.74). This observation is attributed to the partial reduction of GO during $\gamma$-radiation treatment.[26]

Figure 5B shows typical powder X-ray diffraction (XRD) recorded on Pt/GO-GCN, Pt/rGO-GCN, Pt−Sn/GO-GCN, and Pt−Sn/rGO-GCN samples. The $2\theta$ values at 39.6, 46.2, and 68.3° are indexed to (111), (200), and (220) planes of the Pt component (JCPDS 87-0646), respectively. The peaks at 34.3 and 52.04° have been indexed to the SnO$_2$ tetragonal rutile phase in the hybrid composite.[11] The diffractions corresponding to the Sn or SnO$_2$ are less prominent in the diffractogram. The broad peak at ∼27° is due to the interlayered stacking peak (002) of GCN and rGO/GO hybrids.[13] The characteristic peaks due to the graphene oxide or partially reduced graphene oxide (due to $\gamma$-irradiation), rGO, and GCN are seen as broad reflection in XRD.

**2.3. Electrochemical Study of the Composites.** Electrocatalytic activities of these composites for MOR have been studied by cyclic voltammetry on the samples drop-casted on the glassy carbon electrode. Figure 6A shows controlled scan recording in 0.5 M H$_2$SO$_4$. Similar measurements were also carried out on the commercial E-TEK sample under identical conditions. The prominent anodic peaks observed in the Pt redox region (0.4−0.6 V) are attributed to the oxidation of the Pt surface into Pt−OH species. This peak is most prominent in the case of the Pt−Sn/rGO-GCN sample, suggesting a large number of surface hydroxyl species in this sample. The exponential increase in anodic current at extreme positive bias is attributed to triggering of the O$_2$ evolution reaction. On reversing the sweep, a cathodic response is noted in the region 0.7−0.4 V which is due to the reduction of adsorbed Pt−OH on the surface.[7] Interestingly, Pt−Sn/rGO-
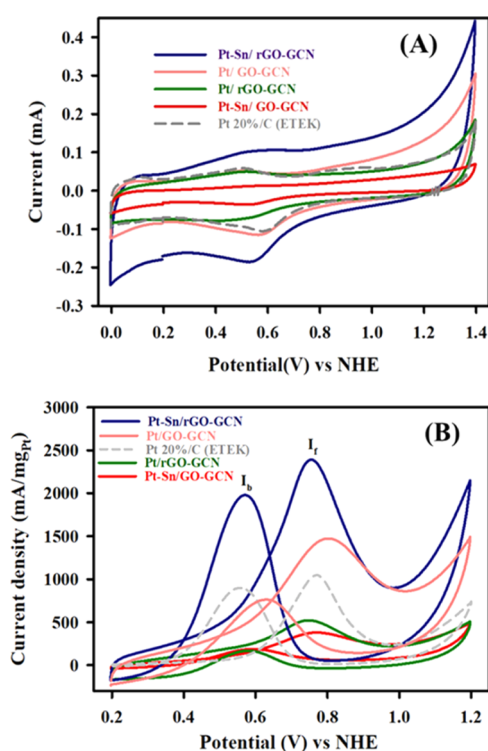


**Figure 6.** Cyclic voltammograms recorded for the composites, Pt−Sn/rGO-GCN, Pt/GO-GCN, Pt/rGO-GCN, and Pt−Sn/GO-GCN, and commercial catalyst (ETEK, Pt 20%). (A) Measurements were carried out on a blank solution of 0.5 M H2SO4 and (B) solution containing 1.0 M methanol and 0.5 M H$_2$SO$_4$. $I_f$ and $I_b$ are the peak anodic current in forward and reverse swipe, respectively.

GCN (black curve) and Pt−Sn/GO-GCN (red curve) show the shift in the −OH reduction peak by −30 mV than the Pt composites (without Sn). Thus, the presence of Sn decreases the activation energy for the reduction of −OH species as inferred. In Pt−Sn/GO-GCN and Pt−Sn/rGO-GCN samples, Sn is predominantly present in two oxidation states, viz., Sn$^{2+}$ and Sn$^{4+}$ (refer XPS spectra in Figure 4C and the discussion therein). These belong to the surface species Sn(OH)$_2$ and Sn(OH)$_4$, respectively. The interaction of Sn−OH with Pt−OH plausibly generates synergy among them and lowers the activation energy for the reduction reaction. This observation is further substantiated by a stronger cathodic peak for −OH reduction than the anodic peaks that belong to Pt oxidation in the case of Pt−Sn composite samples.
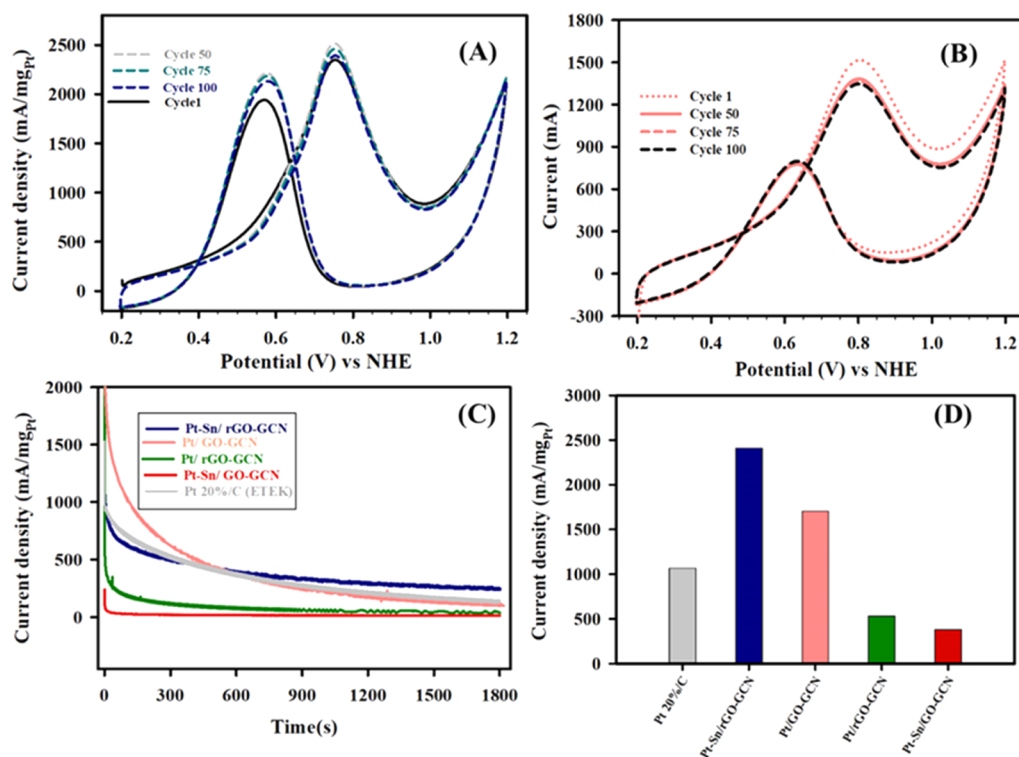
**Figure 7.** Multicycled voltammograms recorded in 1 M methanol and 0.5 M $H_2SO_4$ for (A) Pt−Sn/rGO-GCN and (B) Pt/GO-GCN after various cycle intervals from 1st to 100th cycle. The scan rate was 50 mV/s. (C) Chronamperometry recorded at a step potential of 0.7 V (vs NHE) for all the abovementioned samples. (D) Mass current density values obtained for these samples from the forward anodic peak in CV at the 100th cycle are presented in terms of the histogram.

Similar measurements carried out on Sn-GO-GCN and Sn-rGO-GCN (refer Figure S5 Supporting Information) did not show such features associated to −OH species. Thus, from the CV analysis, we concluded that multiple oxidation states of Sn hydroxides in the composites plausibly help the reduction of Pt−OH in the redox cycles.

Figure 6B shows cyclic voltammetry response for methanol oxidation for all the samples in 1 M methanol and 0.5 M $H_2SO_4$. The current is normalized to per gram of Pt loading (ICP-OES results; refer Supporting Information Table S1). Two anodic peaks, one in the forward scan (marked as $I_f$) and the other in the reverse scan (marked as $I_b$), are noted as a common feature in all the cases. In the previous reports,[27] $I_f$ is attributed to the oxidation of methanol residual intermediates, such as half-way dehydrogenation products and CO. The reverse anodic peak ($I_b$) is correlated to the complete oxidation of these intermediates to $CO_2$. The ratio of the $I_f/I_b$ has been therefore widely used to correlate an extent of poisoning and thus the degree of CO tolerance of the catalysts.[28] However, recent reports[27,29] suggested that the reverse anodic peak (assigned as $I_b$) could be due to the methanol oxidation catalyzed with oxy species on a platinum surface (platinum oxides), which is formed during forward anodic sweep. Thus, the ratio $I_f/I_b$ is corelated to the degree of oxophilicity.

From the CV analysis, the mass-normalized current density (mass activity) of Pt−Sn/rGO-GCN is found to be 2400 mA/$mg_{Pt}$. These values follow the order: Pt/GO-GCN (1477 mA/$mg_{Pt}$) > Pt 20%/C (1045 mA/$mg_{Pt}$) > Pt/rGO-GCN (544 mA/$mg_{Pt}$) > Pt−Sn/GO-GCN (397 mA/$mg_{Pt}$). The activity of Pt−Sn/rGO-GCN is almost double than the activity of commercial E-TEK measured under identical conditions. Comparison of mass activity among all the samples further

suggests that the presence of Sn and r-GO both together is responsible for high mass activity for MOR. The current density is found to be reduced substantially if one of the components (Sn or r-GO) is missing. Based on these results, the plausible mechanism is described as follows.

The mechanism of methanol oxidation involved first dissociative adsorption of methanol and the formation of dehydrogenated intermediates including CO. In the next step, these intermediates react with the adsorbed hydroxyl group on the Pt surface (Pt−OH) and lead to complete oxidation of methanol into $CO_2$. In the acidic pH, the supply of the −OH group from Pt−O species on the surface is insufficient and thus half-reacted intermediates including CO accumulate and poison the catalyst surface. Ru (normally used as a cocatalyst) has multiple oxidation states and provides abundant OH groups even in acidic pH, thus protects the Pt from getting poisoned. Similar to Ru, Sn also has multiple oxidation states which resulted in enhanced response in the Pt−Sn bimetallic system. Our results suggest that substitution of costly Ru with an earth-abundant element, Sn, is equally active in imparting CO tolerance to Pt.

Both Pt−Sn/rGO-GCN and Pt/rGO-GCN show the oxidation peak at 0.75 V (vs NHE) which is 30 mV less positive than the commercial catalyst [Pt 20%/C (0.78 V)]. This shift suggests the less activation energy for MOR on these composites. It may be attributed to the large surface area and high electronic conductivity of the hybrid support, rGO-GCN. Similar measurements carried out for Pt and Pt−Sn loaded on the GO-GCN support gave the oxidation peak at 0.81 V which is 50 mV more positive than for Pt−Sn/GO-GCN. These results imply that the rGO plays an important role in reducing activation energy for oxidation. Similar studies were performed

for controlled samples GO-GCN, rGO-GCN, Sn/GO-GCN, and Sn/rGO-GCN in acidic as well as the solution containing 1 M methanol and 0.5 M $H_2SO_4$ (see Figure S5 Supporting Information). No methanol activities were observed for these controlled samples. These results indicate that Pt is an essential component to break the C−OH bond in the methanol and Sn plays a role as a cocatalyst.

The small initial cathodic currents were noted near starting potential (0.2 V) in all the samples. This feature is also noted for the controlled samples (Figure 6B) and attributed to the charging/discharging current associated to a high surface area of the GO/GCN layer structure.

Figure 7A,B shows multicycle voltammograms recorded for Pt−Sn/rGO-GCN and Pt/GO-GCN, respectively (Figure S7A,B Supporting Information for Pt−Sn/GO-GCN, Pt/rGO-GCN). The peak current density for the forward peak as a function of cycles is used as a rider to judge the dynamic stability. For the Pt−Sn/rGO-GCN, the current density was noted to be 2350 $mA/mg_{Pt}$ which further improved to ca. 2402 $mA/mg_{Pt}$ after the 100th cycle. Improvement in the current density suggests rejuvenation of the catalyst surface during potential cycle due to regeneration of the oxy/hydroxy group provided by Sn upon polarization at positive bias.[20] The variable oxidation state of Sn helps in regenerating hydroxy groups on the surface.

In terms of the added Sn cocatalyst, its interaction with rGO-GCN, the defects on rGO, and self-exfoliation during γ-radiolysis may be attributed to the uniform distribution and intercalation of $Sn/SnO_2$ on rGO. These properties of the composite prevent the agglomeration of the nanoparticles and in turn increase the overall surface area.[30] Such an interaction of the Sn with r-GO has been well-studied for its possible applications in the lithium-ion battery.[31] Also, the favorable Sn with GCN interaction via Sn−N bonding may influence the overall higher activity of Pt−Sn/rGO-GCN combination.[31,32] On the contrary, in the case of Pt/GO-GCN, the current density is degraded from 1514 to 1350 $mA/mg_{Pt}$ at the 100th cycle. Here, the degradation again attributed to the poisoning of the Pt surface due to the scarcity of the −OH group.

The observed higher current density in Pt/GO-GCN as compared to the Pt/rGO-GCN is attributed to the oxy groups in GO which provide favorable sites for the nucleation and growth of Pt nanoparticles. However, as seen in SEM and TEM images (refer Figures 2A and 3A), these features are also responsible for the agglomeration of nanoparticles which is reflected in terms of fast decay in the current density in the case of Pt/Go-GCN as compared to the Pt/rGO-GCN (Figure 7B,C). The lower current density of Pt−Sn/GO-GCN as compared to the Pt/GO-GCN and Pt/rGO-GCN could be attributed to the competition in the reduction of both the metal precursors, $SnCl_2$ ($Sn^{2+}$) and $K_2PtCl_6$ ($Pt^{4+}$) during γ-radiolysis and the available sites for deposition.[33]

To study the current stability of the composites further, chronoamperometry was recorded for the potential step 0.7 V versus NHE, for all the samples, as shown in Figure 7C. The current density of Pt−Sn/rGO-GCN remains stable and higher in longer run as compared to Pt/GO-GCN, Pt (20%)/C, Pt−Sn/GO-GCN, and Pt/rGO-GCN. The high current density is noted at the initial period on the Pt/GO-GCN (pink plot), which is attributed to the capacitive current which was also noted in the CV (refer Figure 6B). The comparison of the mass activities of all the composites is represented by the histogram in Figure 7D. It underlines the better performance of Pt−Sn/rGO-GCN among all the composites and more importantly better than the commercial E-TEK catalyst.

Based on the all the results and analysis, the exceedingly better performance of the Pt−Sn nanoparticle-loaded rGO-GCN hybrid could be correlated to the several factors. First, the higher current density is attributed to the large surface area of reduced graphene oxide and graphitic carbon nitrides which provides better sites for the uniform loading of the Pt and Sn nanoparticles. Furthermore, the defects on the chemically reduced GO could improve the efficient transfer of electrons which transcended into high current density as compared to the other variants. Second, the incorporation of Sn is known to alter the electron density around Pt, thereby weakening the Pt−CO binding energy and enhancing the overall catalytical performances. Additionally, the efficient adsorption of hydroxyl groups from water at lower potential helps to complete oxidation to $CO_2$, thereby showing better control over CO poisoning.[36] Finally, the electron-withdrawing nature of the nitrogen present in the GCN support creates a positive environment around the neighboring carbon and thus favors the formation of OH for efficient oxidation of the CO intermediate, thereby increasing the efficacy of the catalysts.[36] The polymeric nature of the GCN incorporated with rGO could be responsible in prevention of leaching of the catalysts over prolonged use in the acidic media and thus increase the long-term stability of the materials composites, which is reflected in terms of stable current response in the chronoamperogram and dynamic CV measurements.

Overall, Pt−Sn/rGO-GCN shows excellent high current density as compared to the analogues, viz., Pt/GO-GCN, Pt−Sn/GO-GCN, Pt/rGO-GCN, and also commercial Pt (20%)/ETEK. The composites show high stability with the better durability; thus, they could be promising candidates as an anode material for DMFC applications.

## 3. EXPERIMENTAL SECTION

**3.1. Materials.** Graphite powder (Sigma-Aldrich), sodium nitrate, melamine, sulfuric acid (98%), potassium permanganate, stannous chloride (S.D. Fine), sodium borohydride (Sigma-Aldrich), hydrogen peroxide (30% Merck), potassium chloroplatinate (Sigma-Aldrich), and methanol (Thomas bakers) were used as received. All the solutions were prepared in Milli-Q water. Graphene oxide (GO) was prepared from graphite powder using the modified Hummers method.[34] GO was converted to reduced graphene oxide (rGO) with the help of $NaBH_4$, as described in the Supporting Information.

**3.2. Preparation of Graphitic Carbon Nitride.** Graphitic carbon nitride (GCN) was synthesized by autopyrolysis of melamin.[35,36] In brief, 10.0 g of melamine was heated to 500 °C in an inert atmosphere for 2 h with a heating rate of 2 °C $min^{-1}$. The temperature was subsequently increased to 550 °C for another 2 h. The furnace was allowed to cool naturally to room temperature. The resultant yellow powder of the product was recovered and stored under ambient conditions for further use.[35]

**3.3. Preparation of rGO-GCN and GO-GCN Hybrid Composites.** To make the rGO-GCN hybrid composite, dispersion of rGO and GCN (1:1, each 50 mg) in 5 mL water was sonicated for 5−6 h.[37] The resultant dispersion was filtered, dried in an oven, and stored in a vacuum desiccator for the subsequent use. Using a similar procedure, the hybrid of GO-GCN (1:1) was prepared.

**3.4. Preparation and Deposition of Pt/Sn on rGO-GCN and GO-GCN Supports by γ-radiolysis.** γ-Radiolysis was employed to reduce $K_2PtCl_4$ and $SnCl_2$ to their respective metal nanoparticles and their bimetallic composite on chosen substrates.[7,20] In brief, 5 mg of rGO-GCN was dispersed in 10 mL of solution, containing $K_2PtCl_4$ (0.8 mM) and $SnCl_2$ (0.8 mM). Into it, 0.1 mL of 2-propanol was added. The whole mixture was transferred to a 15 mL cuvette and degassed with nitrogen gas for 30 min. The sealed cuvette was exposed to γ-radiation. All the standard operating procedures (SOP) were followed to handle the radioactive source. The optimum results were obtained with a total dose of 1.6 kGy (dose rate of ca. 300 Gy/h). The identical procedure was used to prepare controlled samples, viz., Pt/rGO-GCN, Sn/rGO-GCN, Pt/GO-GCN, Sn/GO-GCN and Pt−Sn (1:1)/rGO-GCN, and Pt−Sn/GO-GCN. After irradiation, the products were filtered, vacuum-dried, and stored under ambient conditions.

We tried to prepare other ratios of Pt/Sn with rGO-GCN and GO-GCN substrates by controlling the starting precursor's concentrations and other parameters. The representative electrochemical measurements in the case of Pt/Sn rGO-GCN samples with varied ratios are presented in Figure S6, Supporting Information. These results brought out that the ratio of Pt/Sn in 2:1 on the rGO-GCN substrate delivered the best electrochemical performance for MOR. Thus, the detailed investigations have been carried out and presented for the 2:1 Pt−Sn rGO-GCN sample. However, a similar strategy did not work in preparation of the GO-GCN sample with varying Pt−Sn ratios. The only stable ratio we could achieve with this substrate was of Pt/Sn in 1:4. Therefore, all the measurements regarding Pt/Sn GO-GCN have been carried out on the 1:4 Pt/Sn GO-GCN sample. The difficulty in getting a Pt-rich sample (2:1 Pt/Sn) in GO-GCN is attributed to the oxide-rich surface of GO which plausibly discourages the deposition of Pt. This interpretation is based on the recent report[22] on electrodeposition of Pt on the $SnO_2$ surface which brought out the role of the oxide layer in inhibiting Pt deposition.

**3.5. Material Characterizations.** A Shimadzu FTIR-8400 spectrophotometer having attenuated total reflection (ATR) accessories was used to record Fourier transform infrared (FTIR) spectra. Powder X-ray diffraction (XRD) patterns of the samples were obtained on a Bruker, D8 Advance X-ray diffractometer (Cu Kα, 40 kV and 40 mA). X-ray photoelectron spectroscopy (XPS) was performed with the help of Thermo Fisher Scientific Instruments having an Al Kα monochromatic source with 6 mA beam current at 12 KV grid bias. Binding energies were calibrated to C 1s at 284.8 eV BE as the reference.

Transmission electron microscopy (TEM) images were recorded using a Technai G2 20 V TWIN transmission electron microscope (20−200 kV), and Raman spectra were recorded on a Jobin Yvon LabRam HR800 Raman spectrometer. All the measurements were carried out at 514.5 nm/30 mW power and for acquisition time 30 s. Field emission scanning electron microscopy (FESEM) images and elemental mappings were recorded using Quanta FEG 450. The actual loading (wt %) and composition of Pt and Sn in the samples were analyzed by inductively coupled plasma optical emission spectrometry (ICP-OES) from Prodigy, Teledyne Leeman Labs; the summarized data are presented in the Supporting Information (Table S1).

**3.6. Electrochemical Characterizations.** Electrochemical measurements were carried out using the potentiostat/

galvanostat workstation model biologic SP300. A conventional three-electrode system having a glassy carbon electrode (GCE diameter $d$ = 3 mm) as a working electrode, Ag/AgCl (3 M KCl) as a reference, and Pt wire loop as counterelectrodes was used. Prior to the experiment, the working electrode was polished over 0.5 μm grade alumina slurry and rinsed with copious amounts of Milli-Q water. 10 μL dispersion of material was drop-casted on the GCE and dried under vacuum. The loading percent of metals was maintained identical for all the sample composites during analysis.

Cyclic voltammograms were recorded on the samples loaded on the GCE, in a 0.5 M $H_2SO_4$ blank electrolyte. The solution was then replaced by 1 M $CH_3OH$ in 0.5 M $H_2SO_4$, without disturbing the electrode system, and MORs were studied.

## 4. CONCLUSIONS

In this work, we presented the synthesis and characterization of the hybrid anode material, that is, Pt−Sn/GO-GCN for DMFC applications. While composing such a cocktail, we carefully chose the methodology to prepare these materials. For example, the support hybrid graphene−graphitic carbon nitride prepared by the sonochemical process, which provided an excellent interaction between them as noted in the Raman analysis. The γ-radiolysis method has been used as it is known to reduce metal salts without any side product and thus delivers debris-free metal surface, essential for catalysis. Also, this method also provides new possibility of scaling up the synthesis for the commercial applications. The hybrid structure of r-GO-GCN provides a large surface area much needed for dispersion of metals. The polymeric nature of GCN saves the composite from getting degraded under dynamic polarization and thus imparts stability. Due to multiple oxidation states, Sn provides abundant surface −OH groups to Pt and decreases the tendency of the Pt catalyst to get poisoned. Besides, Sn is a cost-effective alternative to Ru. Overall, this cocktail catalysts demonstrated excellent performance in terms of high mass activity (double of E-TEK), stability, and less overpotential for the methanol oxidation and proposed to be a potential anode material for future DMFCs.

## ■ ASSOCIATED CONTENT

**ⓈI Supporting Information**

The Supporting Information is available free of charge at https://pubs.acs.org/doi/10.1021/acsomega.1c00114.

Characterizations such as FESEM of GO-GCN and rGO-GCN; EDAX and elemental mapping; composition analysis with respect to Pt and Sn in GO-GCN and rGO-GCN using ICP-OES; XPS spectra; Raman spectra; and cyclic voltammograms recorded for control samples in 0.5 M $H_2SO_4$ and 1 M methanol (PDF)

## ■ AUTHOR INFORMATION

**Corresponding Author**

Santosh K. Haram − *Department of Chemistry, Savitribai Phule Pune University, Pune 411007, India;* ⓞ orcid.org/0000-0002-0618-1215; Email: santosh.haram@unipune.ac.in

**Authors**

Durgasha C. Poudyal − *Department of Chemistry, Savitribai Phule Pune University, Pune 411007, India;* Present Address: Department of Bioengineering, University of

Texas at Dallas, Richardson, Texas 75080, United States.
Email: Durgasha.poudyal@utdallas.edu.

**Rajshree Dugani** — *Department of Chemistry, Savitribai Phule Pune University, Pune 411007, India*

**Banendu Sunder Dash** — *Department of Chemistry, Savitribai Phule Pune University, Pune 411007, India;* Present Address: Department of Chemical and Material Engineering, Chang Gung University, Kwei-San, Taoyuan 33302, Taiwan.

**Manjiri Dhavale** — *Department of Chemistry, Savitribai Phule Pune University, Pune 411007, India*

**Ashis Kumar Satpati** — *Analytical Chemistry Division, Bhabha Atomic Research Centre, Mumbai 400085, India;* orcid.org/0000-0002-2732-8706

Complete contact information is available at:
https://pubs.acs.org/10.1021/acsomega.1c00114

**Notes**
The authors declare no competing financial interest.

### REFERENCES

(1) Debe, M. K. Electrocatalyst Approaches and Challenges for Automotive Fuel Cells. *Nature* **2012**, *486*, 43−51.

(2) Joghee, P.; Malik, J. N.; Pylypenko, S.; O'Hayre, R. A review on direct methanol fuel cells-In the perspective of energy and sustainability. *MRS Energy Sustain.* **2015**, *2*, No. E3.

(3) Tiwari, J. N.; Tiwari, R. N.; Singh, G.; Kim, K. S. Recent Progress in the Development of Anode and Cathode Catalysts for Direct Methanol Fuel Cells. *Nano Energy* **2013**, *2*, 553−578.

(4) Wang, Y.; Chen, K. S.; Mishler, J.; Cho, S. C.; Adroher, X. C. A Review of Polymer Electrolyte Membrane Fuel Cells: Technology, Applications, and Needs on Fundamental Research. *Appl. Energy* **2011**, *88*, 981−1007.

(5) Hampson, N. A.; Willars, M. J.; McNicol, B. D. The Methanol-Air Fuel Cell: A Selective Review of Methanol Oxidation Mechanisms at Platinum Electrodes in Acid Electrolytes. *J. Power Sources* **1979**, *4*, 191−201.

(6) Kamarudin, S. K.; Achmad, F.; Daud, W. R. W. Overview on the Application of Direct Methanol Fuel Cell (DMFC) for Portable Electronic Devices. *Int. J. Hydrogen Energy* **2009**, *34*, 6902−6916.

(7) Joshi, V. S.; Poudyal, D. C.; Satpati, A. K.; Patil, K. R.; Haram, S. K. Methanol Oxidation Reaction on Pt Based Electrocatalysts Modified Ultramicroelectrode (UME): Novel Electrochemical Method for Monitoring Rate of CO Adsorption. *Electrochim. Acta* **2018**, *286*, 287−295.

(8) Dimakis, N.; Navarro, N. E.; Mion, T.; Smotkin, E. S. Carbon Monoxide Adsorption Coverage Study on Platinum and Ruthenium Surfaces. *J. Phys. Chem. C* **2014**, *118*, 11711−11722.

(9) Diao, W.; Tengco, J. M. M.; Regalbuto, J. R.; Monnier, J. R. Preparation and Characterization of Pt-Ru Bimetallic Catalysts Synthesized by Electroless Deposition Methods. *ACS Catal.* **2015**, *5*, 5123−5134.

(10) Kakati, N.; Maiti, J.; Lee, S. H.; Jee, S. H.; Viswanathan, B.; Yoon, Y. S. Anode Catalysts for Direct Methanol Fuel Cells in Acidic Media: Do We Have Any Alternative for Pt or Pt-Ru? *Chem. Rev.* **2014**, *114*, 12397−12429.

(11) Singh, B.; Murad, L.; Laffir, F.; Dickinson, C.; Dempsey, E. Pt Based Nanocomposites (Mono/Bi/Tri-Metallic) Decorated Using Different Carbon Supports for Methanol Electro-Oxidation in Acidic and Basic Media. *Nanoscale* **2011**, *3*, 3334−3349.

(12) Zhao, Y.; Liu, J.; Liu, C.; Wang, F.; Song, Y. Amorphous CuPt Alloy Nanotubes Induced by Na2S2O3 as Efficient Catalysts for the Methanol Oxidation Reaction. *ACS Catal.* **2016**, *6*, 4127−4134.

(13) Zhang, G.; Yang, Z.; Zhang, W.; Wang, Y. Nanosized Mo-doped CeO2 enhances the electrocatalytic properties of the Pt anode catalyst in direct methanol fuel cells. *J. Mater. Chem. A* **2017**, *5*, 1481−1487.

(14) Chang, J.; Feng, L.; Jiang, K.; Xue, H.; Cai, W.-B.; Liu, C.; Xing, W. Pt-CoP/C as an Alternative PtRu/C Catalyst for Direct Methanol Fuel Cells. *J. Mater. Chem. A* **2016**, *4*, 18607−18613.

(15) Huang, H.; Wang, X. Recent Progress on Carbon-Based Support Materials for Electrocatalysts of Direct Methanol Fuel Cells. *J. Mater. Chem. A* **2014**, *2*, 6266−6291.

(16) Mansor, N.; Jorge, A. B.; Corà, F.; Gibbs, C.; Jervis, R.; McMillan, P. F.; Wang, X.; Brett, D. J. L. Graphitic Carbon Nitride Supported Catalysts for Polymer Electrolyte Fuel Cells. *J. Phys. Chem. C* **2014**, *118*, 6831−6838.

(17) Yang, Y.; Chen, J.; Mao, Z.; An, N.; Wang, D.; Fahlman, B. D. Ultrathin g-C3N4 nanosheets with an extended visible-light-responsive range for significant enhancement of photocatalysis. *RSC Adv.* **2017**, *7*, 2333−2341.

(18) Zhang, W.; Fu, Y.; Wang, J.; Wang, X. 3D Hierarchically Porous Graphitic Carbon Nitride Modified Graphene-Pt Hybrid as Efficient Methanol Oxidation Catalysts. *Adv. Mater. Interfaces* **2017**, *4*, 1601219.

(19) Huang, H.; Yang, S.; Vajtai, R.; Wang, X.; Ajayan, P. M. Pt-Decorated 3D Architectures Built from Graphene and Graphitic Carbon Nitride Nanosheets as Efficient Methanol Oxidation Catalysts. *Adv. Mater.* **2014**, *26*, 5160−5165.

(20) Melvin, A. A.; Joshi, V. S.; Poudyal, D. C.; Khushalani, D.; Haram, S. K. Electrocatalyst on Insulating Support?: Hollow Silica Spheres Loaded with Pt Nanoparticles for Methanol Oxidation. *ACS Appl. Mater. Interfaces* **2015**, *7*, 6590−6595.

(21) Chen, X.; Chen, B. Macroscopic and Spectroscopic Investigations of the Adsorption of Nitroaromatic Compounds on Graphene Oxide, Reduced Graphene Oxide, and Graphene Nanosheets. *Environ. Sci. Technol.* **2015**, *49*, 6181−6189.

(22) Schwämmlein, J. N.; Torres, P. A. L.; Gasteiger, H. A.; El-Sayed, H. A. Direct PtSn Alloy Formation by Pt Electrodeposition on Sn Surface. *Sci. Rep.* **2020**, *10*, 59.

(23) Wang, Y.; Djerdj, I.; Smarsly, B.; Antonietti, M. Antimony-Doped Sno2 Nanopowders with High Crystallinity for Lithium-Ion Battery Electrode. *Chem. Mater.* **2009**, *21*, 3202−3209.

(24) Song, H.; Zhang, L.; He, C.; Qu, Y.; Tian, Y.; Lv, Y. Graphene Sheets Decorated with SnO2 Nanoparticles: In Situ Synthesis and Highly Efficient Materials for Cataluminescence Gas Sensors. *J. Mater. Chem.* **2011**, *21*, 5972−5977.

(25) King, A. A. K.; Davies, B. R.; Noorbehesht, N.; Newman, P.; Church, T. L.; Harris, A. T.; Razal, J. M.; Minett, A. I. A New Raman Metric for the Characterisation of Graphene Oxide and Its Derivatives. *Sci. Rep.* **2016**, *6*, 19491.

(26) Gnanaprakasam, P.; Jeena, S. E.; Selvaraju, T. Hierarchical Electroless Pt Deposition at Au Decorated Reduced Graphene Oxide via a Galvanic Exchanged Process: An Electrocatalytic Nanocomposite with Enhanced Mass Activity for Methanol and Ethanol Oxidation. *J. Mater. Chem. A* **2015**, *3*, 18010−18018.

(27) Chung, D. Y.; Lee, K.-J.; Sung, Y.-E. Methanol Electro-Oxidation on the Pt Surface: Revisiting the Cyclic Voltammetry Interpretation. *J. Phys. Chem. C* **2016**, *120*, 9028−9035.

(28) Mancharan, R.; Goodenough, J. B. Methanol Oxidation in Acid on Ordered NiTi. *J. Mater. Chem.* **1992**, *2*, 875.

(29) Hofstead-Duffy, A. M.; Chen, D. J.; Sun, S. G.; Tong, Y. J. Origin of the Current Peak of Negative Scan in the Cyclic Voltammetry of Methanol Electro-Oxidation on Pt-Based Electrocatalysts : A Revisit to the Current Ratio Criterion †. *J. Mater. Chem.* **2012**, *22*, 5205−5208.

(30) Jiang, W.; Wang, W.; Liu, L.; Wang, H.; Xu, Z.; Li, F.; Fu, H.; Lv, H.; Chen, L.; Kang, Y. Sandwich-like Sn/SnO2@Graphene anode composite assembled by fortissimo penetration of γ-ray and

interlamellar limitation of graphene oxide. *J. Alloys Compd.* **2019**, *779*, 856−862.

(31) Zhou, X.; Wan, L.-J.; Guo, Y.-G. Binding SnO2Nanocrystals in Nitrogen-Doped Graphene Sheets as Anode Materials for Lithium-Ion Batteries. *Adv. Mater.* **2013**, *25*, 2152−2157.

(32) Li, T. T.; Xia, L.; Zhang, T.; Zhong, B.; Dai, J.; Tian, X.; Huang, X. X.; Wen, G. Facile Synthesis of Sn/Reduced Graphene Oxide Composites With Tunable Dielectric Performance Toward Enhanced Microwave Absorption. *Front. Mater.* **2020**, *7*, 108.

(33) Lightcap, I. V.; Kosel, T. H.; Kamat, P. V. Anchoring Semiconductor and Metal Nanoparticles on a Two-Dimensional Catalyst Mat. Storing and Shuttling Electrons with Reduced Graphene Oxide. *Nano Lett.* **2010**, *10*, 577−583.

(34) Markad, G. B.; Battu, S.; Kapoor, S.; Haram, S. K. Interaction between Quantum Dots of CdTe and Reduced Graphene Oxide: Investigation through Cyclic Voltammetry and Spectroscopy. *J. Phys. Chem. C* **2013**, *117*, 20944−20950.

(35) Li, X.; Zhang, J.; Shen, L.; Ma, Y.; Lei, W.; Cui, Q.; Zou, G. Preparation and Characterization of Graphitic Carbon Nitride through Pyrolysis of Melamine. *Appl. Phys. A: Mater. Sci. Process.* **2009**, *94*, 387−392.

(36) Shateesh, B.; Markad, G. B.; Haram, S. K. Nitrogen Doped Graphene Oxides as an Efficient Electrocatalyst for the Hydrogen Evolution Reaction; Composition Based Electrodics Investigation. *Electrochim. Acta* **2016**, *200*, 53−58.

(37) Li, Y.; Sun, Y.; Dong, F.; Ho, W.-K. Enhancing the photocatalytic activity of bulk g-C3N4 by introducing mesoporous structure and hybridizing with graphene. *J. Colloid Interface Sci.* **2014**, *436*, 29−36.